# JOURNAL OF CASTING
## & MATERIALS ENGINEERING

JCME

# Contents

# Solidification Process Modeling of Equiaxed Investment Castings with Transient Nonuniform Boundary Condition Definition

**Weston Olson**[ab*] (iD)**, Michael Stemmler**[b] **, Erik Fernandez**[a] (iD)**, Jayanta Kapat**[a] (iD)

[a] University of Central Florida, Center for Advanced Turbomachinery and Energy Research, 4000 Central Florida Blvd, Orlando, FL 32816
[b] Siemens Energy, Gas Services Central Large Gas Turbine Engineering, 11842 Corporate Blvd, Orlando, FL 32817
*e-mail:* weston.olson@siemens-energy.com

## Abstract

The equiaxed investment casting process is a multi-physics problem which requires knowledge from engineers who have expertise in materials, metallurgy, fluid dynamics, thermodynamics, and heat transfer. Process modeling is a tool used by foundries to help predict casting defects such as shrinkage porosity, hot tears, and poor grain structure. The reliability of these predictions is strongly dependent on the accuracy of the thermal boundary conditions set in the model. In this work, a SGT5-2000E Vane 4 cast in Rene 80 nickel-based superalloy was modeled, using the FEA simulation package ProCAST, with two different methodologies. One methodology had very little effort invested into defining the thermal domain. The other methodology involved a thorough consideration of all heat transfer mechanisms acting on the mold. An extensive literature search was performed to define a unique natural convection heat transfer coefficient for each set of surfaces on the mold. The transient boundary layer development was also captured in the definition of the heat conditions. The shrinkage porosity predictions of the models were compared to real-world x-ray data and the transient nonuniform methodology predictions were much more representative than the low fidelity heat transfer methodology predictions. The low fidelity heat transfer model did predict some shrinkage, but not where it appeared in reality. The process modeler will be misdirected by the model results when deriving a solution to the casting process if the real-world physics are not appropriately accounted for in the model. This will be very counterproductive when the foundry is using the model to reduce developmental trials by running trials in model space. References and derived parameters are provided for material properties, emissivity of shell and insulation wraps, and external mold spatially varying heat transfer coefficients.

## Keywords:

solidification process modeling, casting simulation, nickel-based superalloy, equiaxed investment casting, large gas turbine hardware, transient nonuniform heat transfer, natural convection, ProCAST

## 1. INTRODUCTION

Solidification process modeling is practiced by all foundries who manufacture large gas turbine hardware. The material properties, emissivity, heat transfer coefficients, etc. and methodology used by the foundries is considered highly proprietary and strictly confidential. To the best knowledge of the authors, there are no previous publications with respect to equiaxed investment castings of large gas turbine hardware. Zhang et al. [1] performed equiaxed investment casting experiments on a single cored airfoil to derive an interface heat transfer coefficient (IHTC) relationship between the alloy and the shell. The alloy used in his study was aluminum alloy A355 and the ProCAST simulation was validated by experimental results. Szeliga et al. [2] conducted an experiment to determine the interface heat transfer coefficient between IN713C and the ceramic shell mold. The geometry casted was a flat plate oriented horizontally. The findings of the study concluded that the IHTC had a value of 7962 W/(m$^2 \cdot$ K)

at the liquidus temperature sharply decreased during cooling and close to the solidus temperature an increase in magnitude was observed. The secondary peak near the solidus temperature was assumed to be due to mixed oxide scaling at the interface. Sahai and Overfelt [3] investigated the IHTC for various geometries with IN718. The conclusions of their investigation showed that for the cylindrical casting the IHTC varied from 200 to 100 W/(m$^2 \cdot$ K) and for the flat plate it varied from 5000 to 100 W/(m$^2 \cdot$ K). Yang et al. [4] used ProCAST to explore process optimization of an investment cast low pressure turbine blade. The investigation included three different wax pattern configurations and orientations. The blade geometry was hypothetical, and the alloy used was an intermetallic titanium aluminide alloy. The results consisted of a matrix of casting parameters and their corresponding volumes of porosity. Lenda et al. [5] performed solidification process modeling in ProCAST on a simple rectangular casting with the nickel-based superalloy Hastelloy G30. The porosity predictions of the ProCAST model were validated by optical

microscopy which revealed pores in the center of the casting. Miao et al. [6] conducted numerical simulation of an investment casting process for a simple cone like casting with AlSi1 alloy and reported the predicted amount of porosity using ProCAST. Liao et al. [7] investigated the solidification process of a titanium alloy gearbox and validated the ProCAST simulation results to a real-world casting. There are several other studies which use solidification process modeling to validate real-world casting quality and/or optimize the casting process in model space [8–13]. Most of the previous work in the literature consists of applications on simple geometries and no detailed descriptions of the external mold heat conditions are provided. There are also very few studies of solidification process modeling with nickel-base superalloys.

In this work, an actual casting process from a real foundry, Siemens Energy's foundry, was modeled on a large gas turbine hot gas path component, SGT5-2000E Vane 4, and the results were validated against real-world x-ray data. The external mold heat condition modeling methodology is explained in detail for both the low fidelity and the transient nonuniform models. From the fundamental understanding of natural convection, and the extensive studies available in the literature, one knows that the free convection heat transfer coefficient depends on several different factors. These factors include, but are not limited to, the surface temperature or surface heat flux, surface roughness, surface permeability, surface orientation, surface curvature, surface vertical height, etc. From this fundamental knowledge one knows that differently sized, oriented, and shaped surfaces of the mold will have unique external heat transfer coefficients. Hence, the free convective mechanism for investment casting processes will be nonuniform in nature. To the knowledge of the authors, the only transient studies available in the literature are for the cases where the initial temperature difference, between ambient air and heated surface, is zero. For the application of investment castings, this initial condition is not applicable. Assumptions on the transient nature of the boundary layer will have to be made in order to use the existing data in the literature.

Hellums and Churchill [14] provided the first complete solution for transient free convection for any geometry and the results consisted of velocity, temperature, and heat transfer coefficient as a function of time. The application for the study was an isothermal vertical plate. Goldstein and Briggs [15] investigated the penetration distance for a transient developing boundary layer. The study resulted in several correlations for multiple scenarios such as step in surface flux and step change in surface temperature. Salmanpour and Zonouz [16] studied the effect of curvature on steady state heat transfer coefficient numerically. The results concluded that the heat transfer decreases for concave shapes and increases for convex shapes. Bhowmik et al. [17] performed experiments on transient natural convection over a horizontal cylinder. The results of the experiments showed that transient heat transfer strongly depended on position along the cylinder. The stagnation point, or the lowest point of the cylinder, had the least transient heat transfer. Transient heat transfer data was provided as a function of the Fourier number. Eckert and Jackson [18] derived Nusselt number

correlation for a turbulent boundary layer over a constant vertical isothermal surface. Moran and Lloyd [19] investigated the dependency of heat transfer on orientation with respect to gravity. They concluded that the Grashof number can be scaled by cosine of the angle the surface makes with the gravity vector. Vliet and Ross [20] studied the turbulent flow along vertically inclined upward and downward facing plates. They found that for upward facing surfaces the Nusselt number was independent of angle and for downward facing surfaces the Grashof number should be scaled by cosine square of the angle. Hrycak and Sandman [21] studied the heat transfer for a downward facing horizontal surface and provided a correlation for such an orientation. Fishenden and Saunders [22] investigated, and derived a correlation, for an upward facing isothermal surface. Bandyopadhyay et al. [23] studied the transient effects of horizontal isothermal flat plates. The data presented in their work was the Nusselt number as a function of the Fourier number. They also provided the time to reach steady state as a function of Rayleigh number.

Almost all of the correlations provided in the literature are for constant surface or constant heat flux applications but this scenario is not applicable to investment casting. Therefore, one should know that when using these correlations assumptions and approximations must be made for their theoretical application to investment castings. The major deviations from the available studies in the literature and physical phenomena of investment casting transient natural convection heat transfer is the initial condition and the surface boundary condition, with the initial condition being that the heated surface and the ambient temperature are initially the same. The surface boundary condition is a constant surface temperature or constant heat flux.

Understanding the entire heat transfer domain and capturing the various mechanisms in the model setup is imperative for reliable predictions. A summary of the various heat transfer mechanisms at each event in the casting sequence will be presented. The casting setup modeled will be described which includes the wax pattern assembly, gating configuration, insulation wrapping scheme, materials, and the surfaces selected for nonuniform heat condition definition. The natural convection investigations previously referenced will then be used to derive the transient heat transfer coefficients for each spatially varying surface condition. References for the emissivity used for shell and insulation wrap surfaces will also be provided when describing the transient spatially varying heat condition derivation. The definition of the thermal conditions for the low fidelity model will be explained and key differences between both methodologies will be highlighted. The results consist of evaluating the fraction solid and the total shrinkage porosity criteria for both the low fidelity and the transient nonuniform models. Explanation for methodology on evaluating the fraction solid result will also be provided. The explanation will place the emphasis on the law of conservation of mass. The results of both models are compared with real-world x-ray data. The summary of the study, a recommendation for best practices in modeling, and areas which require further investigation are used to conclude this paper.

## 2. HEAT TRANSFER MECHANISMS FOR THE INVESTMENT CASTING PROCESS

Understanding the various heat transfer mechanisms at each event of the casting process is essential in being able to set-up the solidification process model correctly. The investment casting process is a highly transient multi-mode heat transfer process. At each event in the casting process there are different mechanisms of different modes acting on the mold and alloy. Table 1 gives a general outline for a typical investment casting process. Most foundries have some variations between their general casting process and what is outlined in Table 1. The time duration of each of these events will also vary across foundries and across castings within the foundry. The specific sequence of events and their corresponding times is considered proprietary information to the foundry. The casting process modeled in this study consists of the events outlined in Table 1.

**Table 1**
Typical sequence of events for general investment casting process

| # | Event |
|---|-------|
| 1 | Mold transfer from pre-heat oven to furnace |
| 2 | Furnace pump down |
| 3 | Furnace vacuum hold |
| 4 | Mold fill |
| 5 | Furnace vacuum hold |
| 6 | Furnace vacuum break |
| 7 | Mold transfer from furnace to cooling zone |

For all the events there will be internal and external heat transfer mechanisms acting on the mold. The internal mechanisms consist of transient conduction through the shell and insulation wraps along with a thermal contact resistance between contacting surfaces of the insulation wraps. The transient conduction through the mold is defined by the thermal diffusivity, which is a function of the material properties. Specifically, the thermal conductivity, density, and specific heat. The thermal diffusivity plays a very key role in the transient internal heat transfer as it determines how quickly, or slowly, the mold gains, or losses, heat. These internal heat transfer mechanisms will act on the mold during all events of the casting process.

The other internal mechanisms of the mold consist of heat exchange with the alloy. The internal mechanisms of heat transfer between mold and alloy will vary between the mold filling event and the post filling events. For the mold filling event the internal mechanisms consist of radiation, forced convection (for moving fluid), and conduction (for stationary fluid). During the post pour events the mechanism will be conduction until the gap between shell and alloy begins to form. The gap formation is a result of the alloy densification during solidification. According to the conservation of mass, the only way for a liquid to densify into a solid is for there to be a reduction in volume. Hence, the alloy shrinks, and its total volume is reduced. Once the gap between the shell and alloy begins to form, the conduction mechanism converts to a thermal contact resistance mechanism.

This thermal contact resistance between the shell and the alloy is commonly referred to as the interface heat transfer coefficient (IHTC). The interface heat transfer coefficient can be a combination of radiative with convective, or conductive, heat transfer modes. During the vacuum hold the interface heat transfer coefficient will only depend on radiation. The interface heat transfer coefficient strongly depends on the gap width which drives the view factor value for the radiation within the gap. Once the vacuum hold is broken, and air is introduced into the domain, the interface heat transfer coefficient becomes dependent on the total conductance of radiative and convective heat transfer. The convective heat transfer mechanism will be that of natural convection within an enclosure. The reader is referred to work by Yang [24] for details on natural convection within enclosures. The heat transfer coefficient associated with this type of convective mechanism is also dependent on the gap width between the shell and the alloy. Once thermal equilibrium is reached between the gap surfaces and their corresponding boundary layers, the buoyancy forces will diminish. When the air is stagnant within the gap the total conductance for the interface heat transfer coefficient will be a combination of radiation and conduction. The conduction mechanism is also a function of the gap width.

For cored castings there is no gap formation between the alloy and the ceramic core. Since the alloy is compressing onto the core, the heat transfer mechanism between alloy and core is quite different than that of alloy and shell. To the best of the authors knowledge, there are no known studies on the heat exchange between alloy and core during solidification. It is assumed to be a conductive mechanism with a dynamic temperature gradient which is dependent on the rate of contraction of the alloy.

The external mechanisms of the mold exchanging heat with the surroundings will be unique for each event of the casting process. For the mold transfer from pre-heat oven to furnace event the radiative mechanism can be extremely complex. The mold is in motion therefore its view factor, with the surroundings, is constantly changing. Each infinitesimal surface of the mold will have a unique view factor with several other surfaces, each with a different emissivity, a different temperature, and a different surface area. The convective mechanism is also very complex for this event. The mold surfaces are much hotter than the ambient air so there will be natural convection due to the buoyancy forces. The buoyancy forces are the bulk motion of the air due to the density difference near the surface, which is driven by the temperature difference. Depending on the velocity, and overall size, of the mold during transfer, forced convection can also be significant. Therefore, the convective mechanism could consist of mixed forced and free convection heat transfer.

Once the mold is in the furnace and the door is shut, the radiative heat exchange of the mold is with the internal furnace surfaces and with the surfaces of the mold itself. During the pump down stage, air is being pulled out of the furnace and the pressure is decreasing until it reaches a vacuum state. According to the ideal gas law, density is directly proportional to pressure. Therefore, the buoyancy forces which are driven by the density gradient will be decreasing with the pressure during the pump down event. Since it is the buoyancy forces

which drive the bulk motion, the convective mechanism will decrease to a value of zero during the pump down event.

While the mold is filling with the liquid alloy the only external mechanism between the mold and the surroundings is the radiation with the internal furnace surfaces. The radiation will be driven by the view factors between mold surfaces and furnace surfaces, the emissivity, temperature, and surface area of these corresponding surfaces. The external mold surfaces will also be exchanging radiation with other mold surfaces which have a line of site, and a temperature difference, between one another.

During the vacuum break, event air is re-introduced into the domain. Initially there will be a surge of air which is pulled in through the vents of the furnace. Depending on the location of these vents with respect to the mold, this could result in forced convection on the mold. With the furnace being re-pressurized a density gradient at the external mold surfaces will form due to the temperature difference between the surface and the ambient air. This density gradient will drive a transient buoyancy force. Hence, natural convection is expected to be dependent on the transient pressure within the furnace.

For the mold transfer from furnace to cooling zone the radiative mechanism will be the same as the initial mold transfer event. The convective mechanism will also be the same, where it could be a combination of forced and free convection. The key distinction between this event and the initial is that the temperature gradient normal to the surface is driven by the energy released by the alloy during solidification. The radiation exchange may also be with different surfaces at different temperatures and emissivity than the initial event.

Understanding the variations in heat transfer mechanisms for each event and knowing how to account for them in the model setup is critical for obtaining reliable prediction results. Assumptions and approximations must be made to appropriately capture the real-world physics in the model. It would be very unpractical to include the entire surroundings domain during mold transfer into the solidification model. It is left to the process modeler to determine which assumptions and approximations are appropriate and how to apply them accordingly. Regardless, all events which influence the mold temperature should be captured in the model. The temperature gradient within the mold, at the moment that heat exchange with the alloy occurs, is a key influencer on the resulting internal temperature gradient of the alloy. This internal temperature gradient of the alloy greatly influences the quality of the casting and whether it will have an acceptable level of shrinkage or not. The process modelers capability to capture the real-world physics by applying the appropriate assumptions and approximations is considered a necessary skill in setting up the solidification model for reliable predictions.

## 3. CASTING SETUP

The casting setup for SGT5-2000E Vane 4 is now described. To adhere to intellectual property restrictions of the foundry, some of the process parameters will not be specified. The wax pattern assembly is a one-by-one, horizontally oriented casting which is gated from the suction-side mate faces (Fig. 1).

The insulation wrapping scheme consisted of a three-step airfoil wrap with a single layer over the gating system (Fig. 2). The green insulation wrap represents one layer, the pink wrap represents two layers, and the cyan wrap represents three layers.
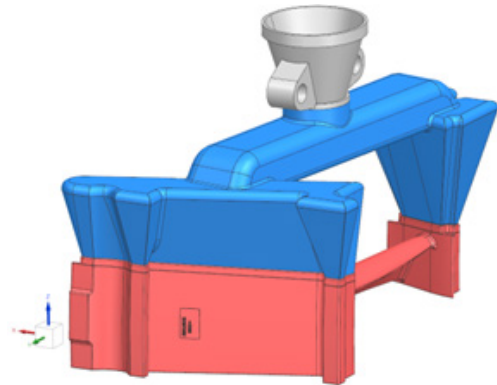


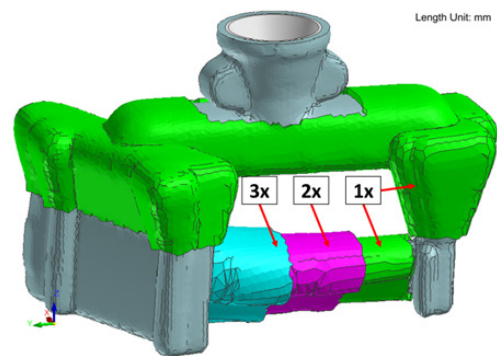**Fig. 1.** Wax pattern assembly



**Fig. 2.** Mold insulation wrapping scheme

The material properties of shell, insulation wraps, and alloy were taken from the ProCAST public database as ceramic refractory mullite, wrap kaowool, and Ni Rene 80, respectively. As summarized in the introduction, natural convection depends on several variables. The variables of interest for this application are the surface size, orientation, curvature, and vertical height. These are defined as the variables of interest since surface roughness and permeability are assumed to be relatively constant across all external surfaces of the mold. The surface temperature is initially constant across the entire external surfaces of the mold after soaking in the pre-heat oven for several hours.

The nonuniform heat transfer coefficient surfaces selected to have a unique heat condition are the convex (CV) and concave (CC) sides of the airfoil, OD and ID platforms (ODPF and IDPF), OD and ID gates (ODGate and IDGate), OD and ID pressure side mate-faces (ODMF and IDMF), and the horizontal top sides of the OD and ID gates (ODHz and IDHz) (Fig. 3). The nonuniform natural convection characteristics for the surfaces previously mentioned are as follows: surface curvature for CV and CC; flat vertical for OD and ID platforms; flat angled for OD and ID gates; horizontal downward facing for OD and ID pressure side mate-faces; and horizontal upward facing for horizontal top sides of OD and ID gates.
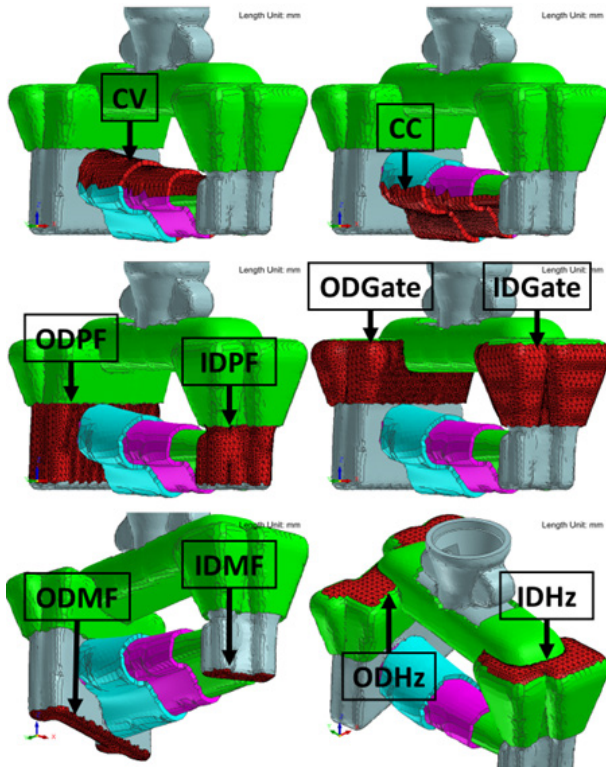
**Fig. 3.** Nonuniform heat condition surfaces

## 4. TRANSIENT NONUNIFORM HEAT CONDITION DERIVATION

There was a unique thermal condition for each region of the mold, the surfaces highlighted in Figure 3. The heat condition in ProCAST consists of a region and a corresponding boundary condition. The parameters used to define the boundary conditions in this study were the heat transfer coefficient (termed as film coefficient in ProCAST) as a function of temperature and time, the emissivity as a function of temperature, the ambient temperature as a constant, with the view factor option enabled. The heat transfer coefficient was defined as a function of temperature because all the correlations found in the literature are a function of the Grashof number, Equation (1).

$$Gr_L = \frac{g\beta(T_s - T_\infty)L^3}{\nu^2} \qquad (1)$$

where:

$g$ – acceleration of gravity [m/s$^2$],
$\beta$ – coefficient of thermal expansion [K$^{-1}$],
$T_s$ – surface temperature [K],
$T_\infty$ – ambient temperature [K],
$L$ – characteristic length [m],
$\nu$ – kinematic viscosity [m$^2$/s].

Defining the heat transfer coefficient as a function of time gives the capability to capture the transient effects associated with boundary layer development, furnace pump down, and

furnace vacuum break events. The emissivity of refractory mullite was defined as a function of temperature and values were obtained from Bauer et al. [25]. Temperature dependent emissivity of kaowool was provided by Jones et al. [26]. Before using the data provided in the literature to derive the nonuniform transient heat transfer coefficients, assumptions must be made so the data may be applicable. Therefore, these assumptions will classify the following derived relationships as approximations and not exact functions. The assumptions, and their reasonings, are as follows:

- All spatially varying heat transfer coefficient surfaces have a negligible temperature variance. They are all insulating materials, highly resistant to temperature change, with the same initial temperature. This allows for application of isothermal correlations provided in the literature.
- Transient heat transfer has an increasing linear relationship until steady state is reached and over/under shoots in boundary layer development are negligible. Without any previous investigations there is no better way to qualify the transient behavior for the initial condition in this application.
- Forced convection during mold transfer is negligible. The mold velocity is relatively low.
- Location of vents in furnace relative to mold will have negligible effect on forced convection during vacuum break.
- Heat transfer coefficient linearly decreases and increases proportionally with pressure for pump down and vacuum break, respectively. The buoyancy forces are driven by the density gradient on the external mold surface, which is dependent on the pressure within the furnace.
- If steady state heat transfer is reached before pump down event, the heat transfer coefficient will decrease linearly from the steady state value to a value of zero. For all transient studies referenced in this investigation there was heat generated in the system. For this application no heat is generated before the mold filling event. Therefore, once steady state values are reached the mold surfaces will further cool and buoyancy forces will decrease.
- Heat flux from mold is constant during solidification.

Results from the investigation by [16] were used to derive a heat transfer coefficient relationship for concave and convex surfaces of the airfoil. The data provided by this study consists of heat transfer coefficients as a function of vertical height and curvature angle for both concave and convex surfaces all with the same temperature difference between wall and ambient. The temperature difference and geometric data was used to calculate the Rayleigh number. The Rayleigh number is the product of the Grashof number and the Prandtl number. This Rayleigh number was used as the reference number to derive a Rayleigh ratio with the Rayleigh numbers associated with the geometry and temperature range of interest. This Rayleigh ratio was used as a scaling factor to scale the Nusselt number provided from [16] at each temperature of interest. The heat transfer coefficient was then calculated by this scaled Nusselt number. Now an approximation, based on experimental data, is available for the heat transfer dependency on temperature for the airfoil surfaces. This dependency is defined by the

dimensionless heat transfer group, Equation (2), as a function of the temperature difference between surface and ambient.

$$h^* = \frac{h}{k}\left(\frac{\nu^2 x}{g\beta(T_s - T_\infty)}\right)^{1/4} \qquad (2)$$

where:

$h$ – heat transfer coefficient W/(m$^2 \cdot$ K),
$k$ – thermal conductivity W/(m $\cdot$ K),
$\nu$ – kinematic viscosity [m$^2$/s],
$x$ – vertical position along wall [m],
$g$ – acceleration of gravity [m/s$^2$],
$\beta$ – coefficient of thermal expansion [K$^{-1}$],
$T_s$ – surface temperature [K],
$T_\infty$ – ambient temperature [K].

The transient dependency approximation was made based off data provided by [17]. The data had steady state heat transfer at a Fourier number of approximately 40. The thermal diffusivity and characteristic length of the system of interest were used with the Fourier number to solve for the time, Equation (3).

$$t = \frac{FoL^2}{\alpha} \qquad (3)$$

where:

$t$ – time [s],
$Fo$ – dimensionless Fourier number [–],
$L$ – characteristic length [m],
$\alpha$ – thermal diffusivity [m$^2$/s].

The authors of [17] state that for any given heat flux, the temperature increased sharply with time. With this statement it is assumed that the temperature of the horizontal cylinder did not vary with time shortly after the heat flux was initiated. The experimental setup in [17] as well as many other studies in the literature differ from the investment casting process in this way. For equiaxed investment castings the mold temperatures will always be in a transient state. Therefore, the time calculated to reach steady state was an average of the steady state Fourier number parameters at preheat temperature to the steady state Fourier number parameters at a temperature halfway to room temperature. This approximation was driven by the fact that the Fourier number is a function of the thermal diffusivity, and the thermal diffusivity is a function of surface temperature.

The characteristic length through which conduction acts was taken as the thickness of a single layer of insulation. This was done because there is an intermediate mechanism at the interfaces of the contacting surfaces of insulation layers. This intermediate mechanism is the thermal contact resistance. Therefore, the same transient time dependency for both convex and concave surface of the airfoil was used. The transient relationship will be defined as the heat transfer coefficient factor as a function of the dimensionless time, Equation (4), for the time interval between pre-heat oven to pump down. The heat transfer coefficient factor is multiplied by the temperature dependent relationship. This factor will essentially represent the development of the transient boundary layer.

$$t^* = \frac{t}{t_{(pre-pump)}} \qquad (4)$$

where $t_{pre-pump}$ is pre-heat to pump down time [s].

According to the assumptions stated at the beginning of this section, the heat transfer coefficient will have linear relationships during the pump down and vacuum break events. The vacuum break duration is less than the time required for the boundary layer to reach steady state. This behavior will be illustrated in one of the following plots.

The average Nusselt number correlation, Equation (5), for turbulent flow along a vertical flat plate provided by [18] was used to define the temperature dependent heat transfer coefficient for OD and ID platform surfaces.

$$Nu_{ave} = 0.0834 Ra^{1/3} \qquad (5)$$

where $Ra$ is dimensionless Rayleigh number.

Correlations derived by [15] were rearranged to solve for the time for the boundary layer to completely penetrate the entire length of the platform surfaces, Equation (6).

$$t_{penetrate} = \sqrt{\frac{x_p}{0.00364 g\beta(T_s - T_\infty)}} \qquad (6)$$

where $x_p$ is penetration distance (vertical length) [m].

Findings by [20] were used to define the heat transfer coefficients for the OD and ID gating surfaces. These surfaces are angled with respect to the gravity vector with heated surfaces facing downward. Therefore, Equation (5) was modified to account for the angle of these surfaces, Equation (7). The application of the cosine squared term is valid for downward facing surfaces angled up to 80 degrees with the gravity vector.

$$Nu_{ave} = 0.0834(\cos^2\gamma Gr_L Pr)^{1/3} \qquad (7)$$

where:

$\gamma$ – angle between surface and gravity vector [°],
$Pr$ – dimensionless Prandtl number.

The gravity term in Equation (6) was modified to account for the angle which the surface makes with the gravity vector, Equation (8).

$$t_{penetrate} = \sqrt{\frac{x_p}{0.00364\cos^2 g\beta(T_s - T_\infty)}} \qquad (8)$$

The Nusselt number correlation derived by [21] was used for the downward facing horizontal surfaces of the pressure side mate-faces, Equation (9).

$$Nu = 0.0017 Ra^{0.596} \qquad (9)$$

The transient relationship was derived from data presented by [23]. The data consisted of the steady state Fourier number as a function of the Rayleigh number. A trendline was created between the data points provided by [23] and this equation was used to populate the Fourier number across the Rayleigh numbers of interest. The time was solved by using Equation (3) where the characteristic length was the ratio of surface area to perimeter and the thermal diffusivity was that of refractory mullite. Since the Fourier number was presented as a function of the Rayleigh number the resulting transient relationships vary for the OD and ID mate-faces due to the large difference in surface size.

The correlation derived by [22] for the Nusselt number of an isothermal upward facing surface was used to define the heat transfer coefficient for the OD and ID horizontal gating surfaces, Equation (10).

$$Nu = 0.54 Ra^{1/4} \qquad (10)$$

The same procedure was used to derive the transient definition as was for the mate-face surfaces. The change in surface size, thermal diffusivity, and length through which conduction occurs have all significantly changed from the mate-face surfaces. Some considerable differences, in transient derivations, between both sets of horizontal surfaces will result from these variations.
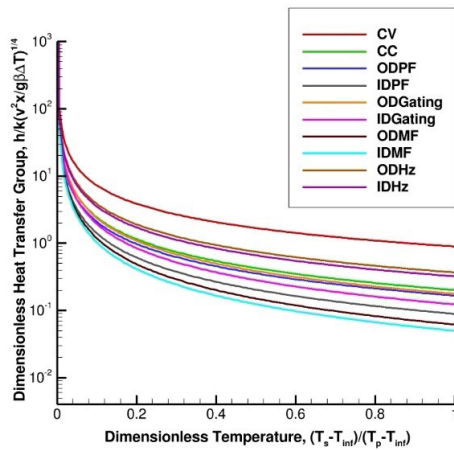


**Fig. 4.** Temperature dependent heat transfer for spatially varying heat transfer coefficient surfaces

Figure 4 illustrates the dimensionless heat transfer group as a function of dimensionless temperature, Equation (11), for all spatially varying heat transfer coefficient surfaces.

$$\theta^* = \frac{(T_s - T_\infty)}{(T_p - T_\infty)} \qquad (11)$$

where $T_p$ is pre-heat temperature [K].

The plot illustrates that each surface will indeed have a unique heat transfer coefficient. Figure 5 illustrates the heat transfer coefficient factor as a function of dimensionless time for all spatially varying heat transfer coefficient surfaces.

Figure 5 shows that each spatially varying heat transfer coefficient surface will also have a unique transient relationship.
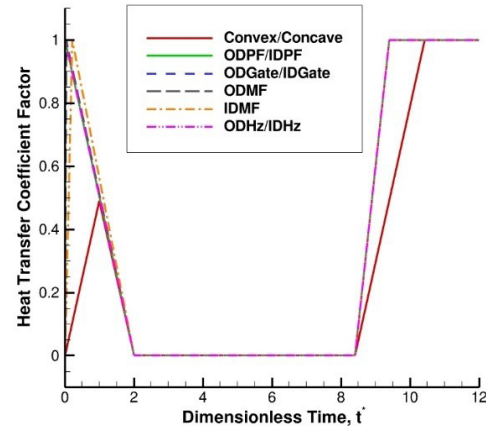
**Fig. 5.** Heat transfer coefficient factor as a function of dimensionless time for spatially varying heat transfer coefficient surfaces

## 5. THERMAL CONDITION DEFINITION FOR LOW FIDELITY MODEL

The low fidelity model had very little effort placed on defining the thermal domain of the system. The emissivity of shell and insulation wraps were taken as constant values and were the first values found through a quick and brief internet search. The emissivity of the shell was defined as a value of 0.5 by reference from [27]. The emissivity of the insulation wraps was defined as a value of 0.9 by reference from [28].

The heat transfer coefficient for the entire external mold surface was defined as a uniform relationship and had a constant value of 10 W/(m² · K) for atmospheric pressure casting events. Hence, the heat transfer coefficient was not unique for each individual surface of the mold. The uniform heat transfer coefficient did capture the transient behavior for pump down and vacuum break but did not consider the initial boundary layer development.

There were several other aspects not taken into consideration in terms of the thermal domain, but were considered in the nonuniform transient heat condition method, such as the transient internal mechanisms of the mold. The low fidelity model had modeled the insulation wraps with the wrap process condition. The wrap process condition only accounts for the external heat transfer mechanisms and does not take into consideration the material properties of the wrap. Therefore, by not accounting for the density and specific heat of the wraps the transient heat transfer nature of the wraps is not accurately considered. The thermal conductivity of the wraps was considered by using a thermal circuit resistance analysis to derive the total heat conductance across the external shell temperature to the ambient temperature. The total heat conductance is simply the reciprocal of the total heat resistance, Equation (12).

$$Z = R_{tot}^{(-1)} = \left( \frac{1}{h} + \frac{nb}{k} \right)^{-1} \qquad (12)$$

where:

$R_{tot}$ – total heat resistance [m²·K/W],
$n$ – number of insulation wraps,
$b$ – thickness of insulation wraps [m].

The main problem with this approach is that the thermal circuit resistance analysis is only valid under steady state conditions and therefore any transient process cannot accurately be analyzed by this method. The nonuniform transient heat condition method on the other hand consisted of wraps represented by individual volumes. Which in return allowed for the assignment of a material and its thermal properties, resulting in a more accurate consideration of the thermal diffusivity.

Another aspect not considered was the radiation exchange during mold transfers. For example, the low fidelity model was modeled as always being inside of the furnace while the radiation enclosure condition had a constant emissivity and constant temperature for the entire casting process. The nonuniform transient heat condition model had a time dependent relationship for both emissivity and temperature to account for the mold transfer events. The nonuniform transient heat condition model also included the mold fixture within the furnace to account for the additional radiation mechanism while the low fidelity had no addition surfaces.

The last key difference between both modeling methodologies is with respect to the interface heat transfer coefficient between alloy and shell. The low fidelity model simply used the relationship for IN738-Mullite from the ProCAST public database and adjusted the mushy zone transition to account for the liquidus and solidus temperatures of Rene 80. The nonuniform transient heat condition model used a relationship found in the literature [2] and not only adjusted mushy zone transition temperatures but also scaled the magnitudes of IHTC to account for the differences in alloy.

There are several key significant differences between both models. The objective of comparing results of both models is to emphasize the importance in attempting to capture all the physics in the model. The scope of the current work is focused on the transient spatially varying heat transfer coefficients. The authors of the current work wished to highlight that other important aspects were not considered in either model. Examples are heat transfer at the wall between alloy and shell during filling, which will be much different than the interface heat transfer which describes the solidification process. Also, local turbulence was not considered. Finally, the IHTC between alloy and shell was only modeled as a function of temperature when we know, by findings from [3], that it also depends on geometry.

## 6. RESULTS AND DISCUSSION

The post processing routine for evaluating the fraction solid criteria for shrinkage porosity predictions is now presented. The fraction solid indicates the state of the alloy in the freezing range. A value of zero implies that the alloy is above the liquidus temperature, and a value of unity implies that the alloy is below the solidus temperature. An intermediate number between zero and unity implies that the alloy is in the mushy zone and dendritic growth has initiated. At some intermediate value there is a limiting fraction of solid between macro-porosity and micro-porosity. Isolated regions of fraction solid below this limit imply the micro-segregation of dendritic growth which results in shrinkage porosity. The correlation between micro-segregation and shrinkage

porosity can be explained by the conservation of mass. If there is an isolated region of dendritic growth, the mass of this isolated region must remain the same. When an alloy solidifies it densifies and the only way that the density can increase is if the volume decreases. For a fixed volume in space the alloy occupying this volume must create pores to densify. Hence, the result is porosity. The limiting value of fraction solid is assumed to be 0.7 for this study.

The real-world x-ray image of the true casting is illustrated in Figure 6. The x-ray detected shrink in the upper airfoil region at approximately between mid-chord and leading-edge. The low fidelity model predictions for isolated regions of fraction solid are shown in Figure 7. After inspection of Figure 7, one can see that the model is predicting an isolated region of fraction solid in the platform airfoil fillet region. Figure 8 illustrates the total shrinkage porosity result for the low fidelity model. The indication in Figure 8 correlates with the isolated region of fraction solid in Figure 7.
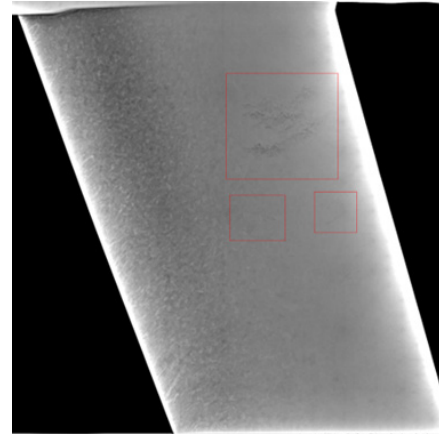


**Fig. 6.** Real-world x-ray image of shrink in upper airfoil region
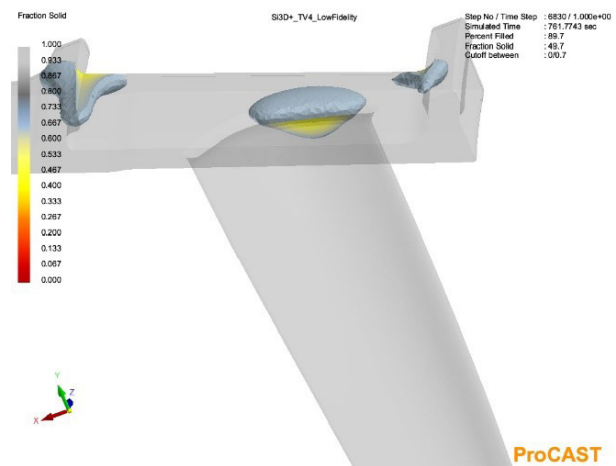


**Fig. 7.** Low fidelity isolated region of fraction solid model predictions

As one can conclude from evaluating both Figure 6–8, the low fidelity model does not capture the defect qualitatively. The defect is being predicted in the airfoil fillet/outer shroud region. The statistics on the defect are an average total shrinkage porosity of 21.48% and a porosity volume of 0.727 cm$^3$.

The predictions of isolated regions of fraction solid for the transient nonuniform model are shown in Figure 9.

**Fig. 8.** Low fidelity shrinkage porosity model predictions



**Fig. 9.** Transient nonuniform isolated region of fraction solid model predictions



**Fig. 10.** Transient nonuniform shrinkage porosity model predictions
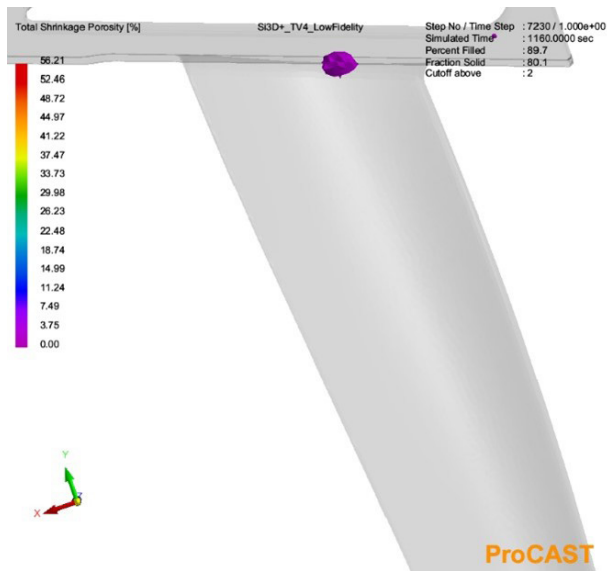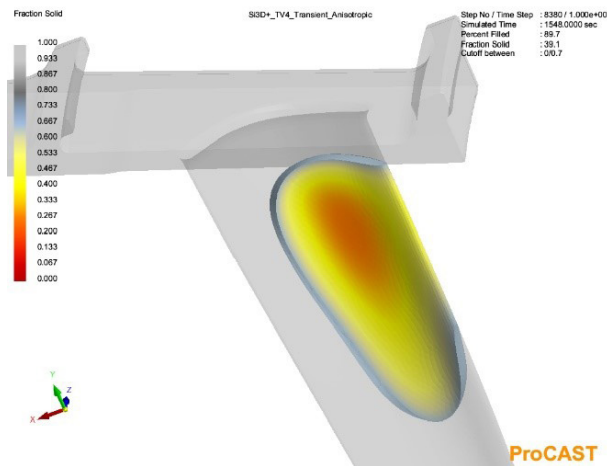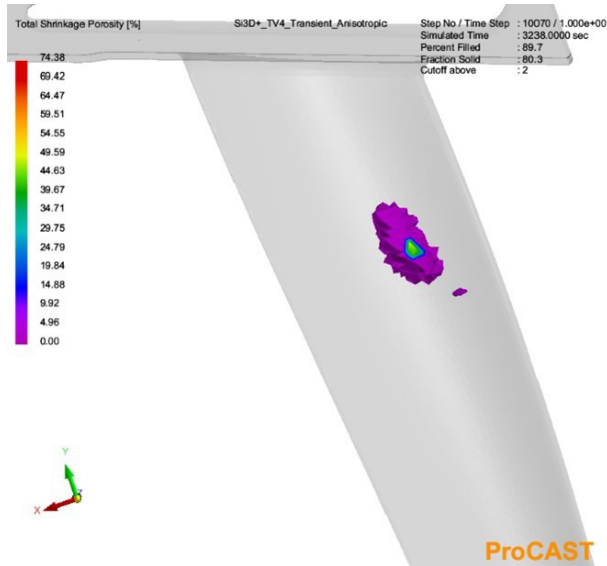
From observation of Figure 9 it is seen that the isolated region of fraction solid corresponds quite well with the indication highlighted in Figure 6. From comparing Figures 6, 9 and 10, it can be concluded that the application of the transient nonuniform methodology results in much more reliable predictions than the low fidelity methodology. The transient nonuniform model qualitatively captures the defect in relatively the same area as seen in the real-world x-ray image. The statistics on the defect are an average total shrinkage porosity of 31.65% and a porosity volume of 8.871 cm$^3$.

The results of both models have been presented to emphasize the importance on capturing the real-world physics in the model definition. The focus of this study was on the nonuniform natural convection heat transfer coefficients, but as mentioned in the previous section there are several other factors that also influence the overall fidelity of the model.

The statistics on the predicted defects were presented but it is recommended to evaluate the model in terms of qualitative measurements and not absolute quantities. There were still a lot of assumptions made on defining the spatially varying heat transfer coefficient conditions, but the application of the methodology was sufficient in generating reliable predictions. With reliable predictions the process modeler can iterate on process conditions, insulation schemes, and gating designs all in model space. This will result in massive amounts of savings in scrap cost and lead times associated with getting components through the product process qualifications and into production for engine set deliveries.

## 7. CONCLUSION

A summary of the main findings and contributions of this work are presented below:

- A thorough detailed explanation of all heat transfer mechanisms and modes is provided for each event of a general equiaxed investment casting process.
- A list of necessary assumptions needed to apply available data in the literature to the application of interest was defined.
- References to an extensive literature review with corresponding correlations used to derive the spatially varying heat transfer coefficients was given.
- Methodology for manipulating the data available in the literature for definition of the transient relationship for spatially varying heat transfer coefficient surfaces was illustrated.
- Low fidelity methodology which should not be practiced was defined and key differences between both methodologies was highlighted and explained in detail.

Due to the insufficient available research associated with the heat transfer mechanisms for equiaxed investment castings, it is planned to run a future experiment with a thermocouple mold. The expected results of the future study will provide the transient heat transfer coefficient development profile for the appropriate initial condition of the application. A continuation of the current work could also be a sensitivity study which would identify a single key aspect, of the transient nonuniform methodology, which is the main driver in

the improvements of the shrinkage porosity predictions. Other potential areas of investigation which could further enhance the fidelity of solidification process modeling predictions are as follows:

- IHTC relationships as a function of vacuum hold, alloy, and shell temperature.
- IHTC relationships between shell and insulation wraps.
- The critical fraction solid at which dendritic micro-segregation occurs and its dependence on alloy properties.
- Heat transfer between alloy and core during solidification.
- Heat transfer between alloy and shell at the wall during filling as a function of momentum and thermal boundary layers.
- Local turbulent heat transfer and its relationship to grain structure.

These are but a few of the topics which still require further investigations. The authors of this work have laid out a methodology which attempts to capture all the heat transfer mechanisms acting during the casting process. The methodology is just one of possibly many which can be used to accurately predict shrinkage porosity defects.

## REFERENCES

[1] Zhang W., Xie G., & Zhang D. (2010). Application of an optimization method and experiment in inverse determination of interfacial heat transfer coefficients in the blade casting process. *Experimental Thermal and Fluid Science*, 34(8), 1068–1076. Doi: https://doi.org/10.1016/j.expthermflusci.2010.03.009.

[2] Szeliga D., Kubiak K., Ziaja W., Cygan R., Suchy J.S., Burbelko A., Nowak W.J. & Sieniawski J. (2017). Investigation of casting-ceramic shell mold interface thermal resistance during solidification process of nickel based superalloy. *Experimental Thermal and Fluid Science*, 87, 149–160. Doi: https://doi.org/10.1016/j.expthermflusci.2017.04.024.

[3] Sahai V. & Overfelt R. (1995). Contact conductance simulation for alloy 718 investment castings of various geometries. *Transactions of the American Foundrymen's Society*, 103, 627–632.

[4] Yang L., Chai L.H., Zhang L.Q. & Lin J. (2013). Numerical simulation and process optimization of investment casting of the blades for high Nb containing TiAl alloy. *Materials Science Forum*, 747–748, 105–110. Doi: https://doi.org/10.4028/www.scientific.net/MSF.747-748.105.

[5] Lenda O.B., Tara A., Jbara O., & Saad E. (2019). Numerical simulation of investment casting process of nickel-based alloy. In: *MATEC Web of Conferences*, Vol. 286, p. 03005. EDP Sciences.

[6] Miao L., Tang Z., Zhang D., Meng F., Wang J. & Li X. (2021). Investment casting simulation and analysis of shell AlSi11 alloy part. *Journal of Physics: Conference Series*, 2002(1), 012040.

[7] Liao Q., Ge P., Lu G., Yang S., Ye W., Gao J. & Luo X. (2022). Simulation study on the investment casting process of a low-cost titanium alloy gearbox based on ProCAST. *Advances in Materials Science and Engineering*, 19, 1–10. Doi: https://doi.org/10.1155/2022/4484762.

[8] Malik I., Sani A.A. & Medi A. (2020). Study on using casting simulation software for design and analysis of riser shapes in a solidifying casting component. *Journal of Physics: Conference Series*, 1500(1), 012036.

[9] Kishimoto A., Takagawa Y. & Saito T. (2020). Prevention technology of shrinkage using actual casting test and casting simulation. In: H. Okada, S.N. Atluri, *Computational and Experimental Simulations in Engineering: Proceedings of ICCES2019*. Springer International Publishing, pp. 827–837.

[10] Barot R.P. & Ayar V.S. (2020). Casting simulation and defect identification of geometry varied plates with experimental validation. *Materials Today: Proceedings*, 26(2), 2754–2762. Doi: https://doi.org/10.1016/j.matpr.2020.02.575.

[11] Kang J., Wang J., Shangguan H., Zheng L., Deng C., Hu Y. & Yi J. (2020). Modeling and simulation of the casting process with skeletal sand mold. *Materials*, 13(7), 1596. Doi: https://doi.org/10.3390/ma13071596.

[12] Domeij B., Belov I., Fourlakidis V. & Dioszegi A. (2022). Implementation and validation of casting simulation methodology for diagnostics of lamellar graphite iron. *International Journal of Metalcasting*, 17(3), 1–11. Doi: https://doi.org/10.1007/s40962-022-00892-9.

[13] Haldar P. & Sutradhar G. (2021). Simulation and validation of castings in shop floor. In: Z. Abdallah & N. Aldoumani (Eds.), *Casting Processes and Modelling of Metallic Materials*. IntechOpen, pp. 53–69, https://www.intechopen.com/chapters/74553.

[14] Hellums J.D. & Churchill S.W. (1962). Transient and steady state, free and natural convection, numerical solutions: Part I. The isothermal, vertical plate. *AIChE Journal*, 8(5), 690–692. Doi: https://doi.org/10.1002/aic.690080525.

[15] Goldstein R.J. & Briggs D.G. (1964). Transient free convection about vertical plates and circular cylinders. *ASME Journal of Heat and Mass Transfer*, 86(4), 490–500. Doi: https://doi.org/10.1115/1.3688728.

[16] Salmanpour M. & Zonouz O.N. (2008). Numerical comparison of the effect of concave and convex curvatures over the rate of heat transfer from a vertical wall in natural convection flow. *Heat Transfer Research*, 39(6), 549–558. Doi: https://doi.org/10.1615/HeatTransRes.v39.i6.90.

[17] Bhowmik H., Gharibi A., Yaarubi A. & Alawi N. (2019). Transient natural convection heat transfer analyses from a horizontal cylinder. *Case Studies in Thermal Engineering*, 14, 100422. Doi: https://doi.org/10.1016/j.csite.2019.100422.

[18] Eckert E.R.G. & Jackson T.W. (1950). *Analysis of turbulent free-convection boundary layer on flat plate* (No. NACA-TN-2207). Washington: National Advisory Committee for Aeronautics.

[19] Moran W.R. & Lloyd J.R. (1975). Natural convection mass transfer adjacent to vertical and downward-facing inclined surfaces. *ASME Journal of Heat and mass Transfer*, 97(3), 472–474. Doi: https://doi.org/10.1115/1.3450404.

[20] Vliet G.C. & Ross D.C. (1975). Turbulent natural convection on upward and downward facing inclined constant heat flux surfaces. *ASME Journal of Heat and mass Transfer*, 97(4), 549–554. Doi: https://doi.org/10.1115/1.3450427.

[21] Hrycak P. & Sandman D. . (1986). Radiative and free-convective heat transfer from a finite horizontal plate inside an enclosure. In: *14th Space Simulation Conference: Testing for a Permanent Presence in Space.* NASA Conference Publication 2446, National Aeronautics and Space Administration, pp. 42–62.

[22] Fishenden M. & Saunders O.A. (1950)., *An Introduction to Heat Transfer*. London: Oxford University Press.

[23] Bandyopadhyay K., Oosthuizen P.H. & Li Q. (2023). A numerical study of unsteady natural convection from two-sided thin horizontal isothermal plates. In: *Proceedings of the 10th International Conference on Fluid Flow, Heat and Mass Transfer (FFHMT'23)*, paper no. 108. Doi: https://doi.org/10.11159/ffhmt23.108.

[24] Yang K.T. (1987). Natural convection in enclosures. In: S. Kakac, R.K. Shah & W. Aung (Eds.), *Handbook of Single-Phase Convective Heat Transfer*. New York: John Wiley, pp. 13.1–13.51.

[25] Bauer W., Moldenhauer A. & Platzer A. (2005). Emissivities of ceramic materials for high temperature processes. *Optical Diagnostics*, 5880, pp. 263–272. SPIE. Doi: https://doi.org/10.1117/12.624512.

[26] Jones J.M., Mason P.E. & Williams A. (2019). A compilation of data on the radiant emissivity of some materials at high temperatures. *Journal of the Energy Institute*, 92(3), 523–534. Doi: https://doi.org/10.1016/j.joei.2018.04.006.

[27] Hakes S. (2011). How space shuttle technology improves crown emissivity. *Glass International*, https://www.glass-international.com/content-images/news/FIC.pdf [accessed: 22.11.2023].

[28] Unifrax LLC. (2017). Fiberfrax® Blanket and Mat Products. *Product Information Sheet*. http://buyinsulationproducts.com/files/126993874.pdf [accessed: 22.11.2023].

# Characterisation of Polacrylate-Polysacharide System.
# Part I. Infrared Structural Studies

**Karolina Kaczmarska\***⬤, **Mateusz Śmietana, Dariusz Drożyński**⬤, **Faustyna Woźniak**⬤, **Artur Bobrowski**⬤

AGH University of Krakow, Faculty of Foundry Engineering, Reymonta St. 23, 30-059 Krakow, Poland
*\*e-mail: karolina.kaczmarska@agh.edu.pl*

**Abstract**

For the prepared polymer systems based on an poly(acrylic acid) and a colloidal solution of native starch, a series of IR (FTIR) structural studies and tests under heating conditions (ATR-FTIR) were carried out. Two components from the group of native starch of different biological origin (potato, cassava) were selected. The analysis of the collected results was aimed at assessing the effect of the biological origin of the starch on the structure, thermal sensitivity of the acrylic polymer-based system. On the basis of interaction effects occurring in the obtained synthetic polymer-natural polymer systems, the validity of mixing selected components to obtain composition was verified.

**Keywords:**

material engineering, hydrogel, native starch, polyacrylic acid, spectroscopy FT-IR

## 1. INTRODUCTION

Hydrogels are considered as a group of polymeric materials whose hydrophilic structure enables to retain large amounts of water in three-dimensional networks. Today, hydrogels continue to fascinate material scientists and researchers, and great progress has been made in their formulations and applications. The wide range of components, their mixability and origin mean that hydrogel materials are used in many industrial and environmental areas.

### 1.1. Hydrogels

A hydrogel is a gel in which the dispersed phase is water and the forming phase (gelling agent) may be a polymer – either natural (e.g. acacia gum, carrageenan, agar) or modified and synthetic (polysiloxanes, synthetic rubbers) [1, 2].

A number of methods for classifying hydrogels are encountered in the literature. Based on the type of interactions between the molecules that form the cross-linked gel structure, we distinguish between physical and chemical gels. In the latter, the macromolecules are linked to each other by covalent bonds, making these hydrogels usually thermally and chemically resistant. The structure of physical gels can be maintained by hydrogen bonds, molecular bonds, or ionic interactions. Under the influence of other substances, with a change in pH, or at elevated temperatures, physical gels can change to a sol state. This phenomenon is usually reversible. Depending on the chemical composition of the substance that forms the three-dimensional network, hydrogels are divided into organic and inorganic. Based on the source of the polymer that forms the solid phase, hydrogels

are classified into natural and synthetic. Another division of hydrogels involves the possession (or not) of an electrical charge in the polymer networks. Polymers that are ionisable or contain ionic groups are called polyelectrolytes. Among them we distinguish hydrogels: anionic (pectin, hyaluronic acid, alginic acid); cationic (chitosan, polylysine); amphoteric (starch, gelatine, collagen). They are also classified according to their structure, i.e. amorphous, which are formed due to the random linking of polymer chains, and semicrystalline, in which crystalline regions are present [3].

The properties of polymer hydrogels depend on many factors, including the type of polymer, the degree of cross-linking, the chemical composition of the liquid to be absorbed and also the fineness of the product (dispersed phase). Hydrogels can exist in a variety of physical forms including solids. The components used also determine the biocompatibility, non-toxicity, ability to absorb large quantities of water, flexibility, and chemical and thermal resistance that hydrogels usually possess [3]. Hydrogels are also characterised by their permeability, which is largely dependent on the porosity, size, distribution, and curvature of the pores. The more compact the hydrogel exhibits, the lower the permeability than the in the case of a broken down structure, i.e. larger pores, more pores.

As already indicated – hydrogels form a three-dimensional cross-linked structure. The polymer network (spatial structure) is formed due to the existence of chemical bonds between the polymer chains. This process is called chemical crosslinking. In a cross-linked hydrogel, we can distinguish between single covalent bond links, molecular entanglements and multifunctional links [3]. Crosslinking of polymeric hydrogels can be carried out by chemical and physical

methods. Chemical methods include crosslinking by radical polymerisation, chemical reaction of complementary groups, reaction with aldehydes, addition reaction, condensation reaction, by irradiation, using enzymes. Physical crosslinking methods occur by: ionic interaction, crystallisation, by the formation of stereocomplexes, by the formation of hydrogen bonds, by interaction with proteins [4].

New areas of material application are forcing innovative approaches in the design of hydrogels with much improved mechanical, sorptive, superporous properties and composed of chemically or even genetically modified components. Hydrogels, due to their diverse properties, are used in the chemical industry (for cosmetics), pharmaceutical industry (as wound plasters), biotechnology (replacing collagen, as contact lenses), food (for frozen food packaging), cosmetics (for soap production), metallurgy (heavy metal sorbents), as well as in environmental protection, agriculture and horticulture (agro-gels, soil-moisture granules) [4, 5].

It seems that there is a possibility to apply polymeric hydrogels also in casting, or rather mould technology. Namely, the application of this material can be related, for example, to obtaining models for moulds (or parts of their construction), as due to their properties they are interesting materials from the perspective of 3D printing technology [6, 7].

In simple terms, 3D printing technology using hydrogels involves applying thin layers of material in succession until the expected shape of the object is achieved. Advanced technologies make it possible to print a 'fibre' up to ten times thinner than a sheet of paper. This makes it possible to apply layers of material more precisely and to create complex and delicate forms, shapes (models). Literature data shows that parts printed from hydrogels are less brittle and more flexible. Moreover, after printing the desired shape, it is possible to subject the hydrogel object to drying, thanks to which water is removed from the object and the form itself visibly shrinks, while it returns to its original shape after soaking in water. Such properties are mainly used in medicine [7, 8].

Hydrogels are of interest based on both natural and synthetic components, with the latter gradually dominating the market with technological progress due to higher water absorption and long service life. The most popular synthetic base polymers of hydrogels are acrylic polymers, whose monomers of primary importance are acrylic acid, methacrylic acid, acrylamide, and their derivatives. Among natural polymers, polysaccharides and their modifiers are mentioned as components of hydrogels. In the case of this group of polymers, the type of biological raw material from which it is obtained may have a significant influence on its properties. In the following section, we discuss in more detail a polymer from the group of synthetic acrylic polymers: poly(acrylic acid) and a natural polymer: native starch.

## 1.2. Acrylic polymers – poly(acrylic acid)

Acrylic polymers are mainly obtained from the radical polymerisation reaction of acrylic acid, methacrylic acid or nitrile and amide ester derivatives. The monomer of the poly(acrylic acid) chains is acrylic acid – the simplest unsaturated carboxylic acid [1]. Poly(acrylic acid) is a weaker acid compared to its monomer. It shows solubility in polar compounds (water, lower alcohols, ethylene glycol), while it is insoluble in saturated and aromatic hydrocarbons. Solubility is reduced by an increase in molecular weight and increased by an increase in temperature. Poly(acrylic acid) is a polymer with high water-binding capacity and has hydrogel characteristics. Poly(acrylic acid) is most often used as an intermediate in the production of polymers used in many industries, e.g. automotive, construction, toys and paper. These plastics are used in the production of paints, adhesives, and adhesive tapes. They are used in dentistry, prosthetics, and orthopaedics as the basis for bone cement. In addition, the material can be used in the construction of hearing aids and the manufacture of contact lenses. It is also used as a thickening, dispersing and binding agent [9, 10]. Poly(acrylic acid) and its derivatives are also used in casting mould technology. They can be the main component of a casting binder, imparting strength to the mould, reducing the oscillation of moulding and core masses cured both chemically and physically. Finally, it acts as a binding and stabilising material in protective coatings [11–13].

## 1.3. Polysaccharide – native starch

Native (natural) starch is the most widespread polymer of the polysaccharide group in nature. It is found in potato tubers, flowers, stems, cereals, roots, and fruits. Its main function is as a storage element in plants – it stores energy, which, helps the plant to survive in difficult growth conditions (fluctuating temperature, drought). It is also a source of carbon (building material) for young germinating plants. There are two forms of starch in plant cells: storage starch and assimilatory starch. Assimilatory starch is synthesised in the leaves and is then broken down to sucrose, and sucrose itself is converted by biosynthesis to spare starch [14].

At the boundary between physical and chemical characteristics lies the ability of starch to gel (colloid). This process is related to the swelling of starch grains due to the action of water under higher temperature conditions (50–70°C). Solvent heating is necessary because native starch does not dissolve in cold water. When heated, the inter- and intramolecular hydrogen bonds of the starch components are broken. Water leaches out the amylose to form a colloid. The gelatinization of starch, the swelling and gelling process, the viscosity and stability of the gel depend on the origin (Table 1) and how the starch was extracted from the material [15].

**Table 1**
Example of gelatinisation temperature of starch of different botanical origin [15]

| Starch type | Swelling onset temperature [°C] | Gelatinisation onset temperature [°C] | Full gelatinisation temperature [°C] |
|:---:|:---:|:---:|:---:|
| potato | 46.0 | 59.0 | 62.5 |
| wheat | 50.0 | 65.0 | 67.5 |
| rice | 54.0 | 59.0 | 61.0 |
| corn | 50.0 | 55.0 | 62.5 |
| cassava | 49.0 | 58.0 | 63.0 |

As a result of gelatinisation, the crystallinity of the starch changes (semicrystalline to amorphous). Subsequently, during the storage period of the starch gel in amorphous form, the amylose molecules are organised by aggregation into a double helix through intermolecular hydrogen bonds. Such aggregates are secreted as dendrites and are insoluble in water. This process is called retrogradation. Its consequence is a reduction in the intermolecular spaces, which pushes water out of the gel (syneresis), which means dehydration of this material [15]. Retrogradation of starch colloids can occur over an extensive temperature range (−20°C to 100°C), but is most intense between −8°C and 8°C [16].

Because gel syneresis and retrogradation can cause the deterioration of food products, starches are subjected to various types of modification. The aim is to adapt the properties of the starch to the parameters of the technological process in order to produce a product with the desired shelf life, stability during application and storage. Among the physical methods of starch modification, a distinction is made between gelling, extrusion, agglomeration and combination methods [17]. Chemical modification processes are carried out by degradation of the polymer chain (hydrolysis, dextrination, oxidation), as well as by substitution reactions (esterification, etherification). The last and one of the most important methods of starch modification in the starch processing industry is crosslinking. This involves the replacement of weak hydrogen bonds with strong covalent bonds [18].

This paper presents a structural analysis of polyacrylic hydrogels with the addition of gelatinised native starch of different botanical origin (a combination of synthetic and natural polymers). A comparative analysis taking into account the influence of the botanical origin of starch on the hydrogel structure, including under elevated temperature conditions, has been carried out. The characterisation of the studied hydrogels will be useful in planning the technology of moulding objects in 3D printing technology.

## 2. EXPERIMENTAL

### 2.1. Materials

Based on literature data [19–21] poly(acrylic acid) (PA; PA80 – 35% aqueous solution/BASF) was selected for the preparation of polymer hydrogels. The polyacrylate hydrogel component was selected as:

- $S_P$ – native (natural) potato starch (Trzemeszno S.A., Poland), white powder, odourless; moisture content 18.6%;
- $S_C$ – native (natural) cassava starch (Cock Brand Marque Deposee, Thailand), white powder, odourless; moisture content of product 13.0%.

The solvent in hot-prepared colloidal solutions of natural starches – starch gels, was distilled water (Avantor Performance Materials Poland S.A.).

### 2.2. Samples natural starch solutions preparation

The preparation of PA+S hydrogels required the prior preparation of colloidal solutions of natural starches (starch gels). On the basis of literature data [15]. The full gelatinization temperature of the potato and cassava starches was set at about 63°C. These data are relevant to the preparation of aqueous starch solutions.

A weighed portion of undried native starch in solid form (powder) was introduced into a glass vessel with cold distilled water at a weight ratio leading to a 10% solution. Then the whole was placed in a laboratory heating device with the power adjusted to reach the temperature of full gelatinisation of potato and cassava starch (~63°C). The temperature of the sample was controlled with a digital laboratory thermometer TH101.

For both types of starch, gelatinisation was carried out in an identical manner. The viscous solutions obtained were then directed to the preparation of polyacrylate hydrogels. Due to the possibility of the retrogradation process occurring during the storage of the colloidal starch solutions, the next steps of the study plan, i.e. the preparation of the systems with the acrylic polymer, were carried out within 2 h of the preparation of the gel.

### 2.3. Preparation of hydrogels

The experimental part of the paper focused on the study of two polyacrylate hydrogels based on polyacrylic acid water solution and gelatinised native starches (see Section 2.2). The ingredients ratio was: 1 parts by weight PA to 3.5 parts by weight starch gel. The hydrogels are designated in the text as follows:

- H-PA+$S_P$ – PA-based polyacrylate hydrogel containing gelatinised potato starch (Fig. 1a);
- H-PA+$S_C$ – PA-based polyacrylate hydrogel containing gelatinised cassava starch (Fig. 1b).

Approximately 1 g of H-PA+$S_P$ and H-PA+$S_C$ hydrogel was left in the conditioning chamber for 24 h at 25°C and 30–45% humidity to partially dry.
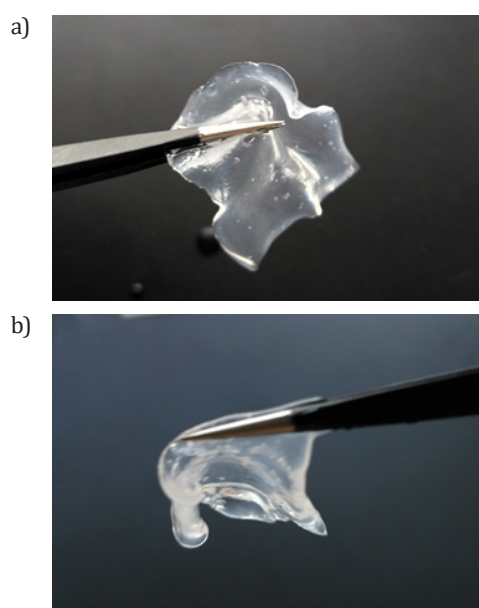


**Fig. 1.** View of a polyacrylate hydrogel object with starch after water adsorption: a) H-PA+$S_P$; b) H-PA+$S_C$

## 2.4. Methods

### Fourier transform transmission spectrosopy

Recording of the spectra of the obtained hydrogels and their components was carried out as follows. The spectra were measured using the company's Digilab Excalibur FTS 3000 Mx Fourier spectrometer, in the range corresponding to mid-infrared. Two measurement techniques available to IR spectroscopy were used: transmission and reflection, using appropriate attachments.

In the Varian PRO software panel, the spectrum measurement parameters were established: wavenumber range 4000–400 cm$^{-1}$, spectral resolution of the apparatus 4 cm$^{-1}$, number of measurements to be averaged – 32 scans. Preparation ofthe KBr pellet started with weighing out 200 mg of potassium bromide KBr using an electric balance and grinding it in an agate mortar. KBr was then poured into a special matrix and pressed under 8 tonnes, using a hydraulic press. A pellet with a diameter of 10 mm and a thickness of about 1 mm was made. The resulting KBr pellet was placed in the spectrometer attachment and the background was measured. Next, another pastille was then prepared by weighing out 200 mg of KBr and adding about 2 mg of the test substance. The hydrogels and components investigated in this study have the consistency of a viscous liquid, so a small amount was applied directly to a pellet of pure potassium bromide. The pastille thus obtained as a sample carrier was placed in a spectrometer and the spectrum recorded.

### Attenuated total reflection Fourier transform infrared (ATR-FTIR) spectroscopy

Studies of the effect of increasing temperature on the structure of the obtained hydrogels were carried out using the reflection multiple weakened reflection – the attenuated total reflection Fourier transform infra-red (ATR-FTIR) technique.

The temperature controller was set to an initial temperature of 25°C. In the Varian PRO software panel (which controls the operation of the Digilab Excalibur FTS 3000 Mx Fourier spectrometer), the following measurement parameters were set: wavenumber measurement range: 4000–600 cm$^{-1}$, spectral resolution of the instrument: 4 cm$^{-1}$, number of measurements to be averaged: 64 scans. After temperature stabilisation on the instrument, the background spectrum (air) was measured. The sample (1–2 mg) was placed with a Pasteur pipette on the appropriate surface of the attachment. The spectrum of the sample was recorded at 25°C and were repeated at 50°C, 75°C, 100°C, 125°C, 150°C, 175°C and 200°C, each time the temperature on the instrument was set by the controller; recording of the spectrum was initiated 30 s after reaching the set temperature on the instrument.

## 3. RESULTS AND DISCUSSION

### 3.1. Structural characteristics of polyacrylate hydrogels with natural starch

Figure 2 summarises the IR spectra of polyacrylate hydrogels and their components. Not only the liquid, freshly prepared hydrogel, but also the hydrogel dried in air for 24 h (in solid form) was tested.

The analysis of the FTIR spectra shows that natural potato starch and cassava starch in their initial form have a similar chemical structure. The maxima of the characteristic bands were located in a similar range of wave numbers, indicating that the same groupings are present in both samples. The difference in the shape of the spectra was located in the wavenumber range 3800–3000 cm$^{-1}$ – two maxima on the $S_P$ spectrum and one on the $S_C$ spectrum – which may be related to the different proportion/proportion in the starch structure of the natural intra- and intermolecular bonds in the starch polymer chains and the crystalline and amorphous fraction (Fig. 2, spectra 1a and 1b).
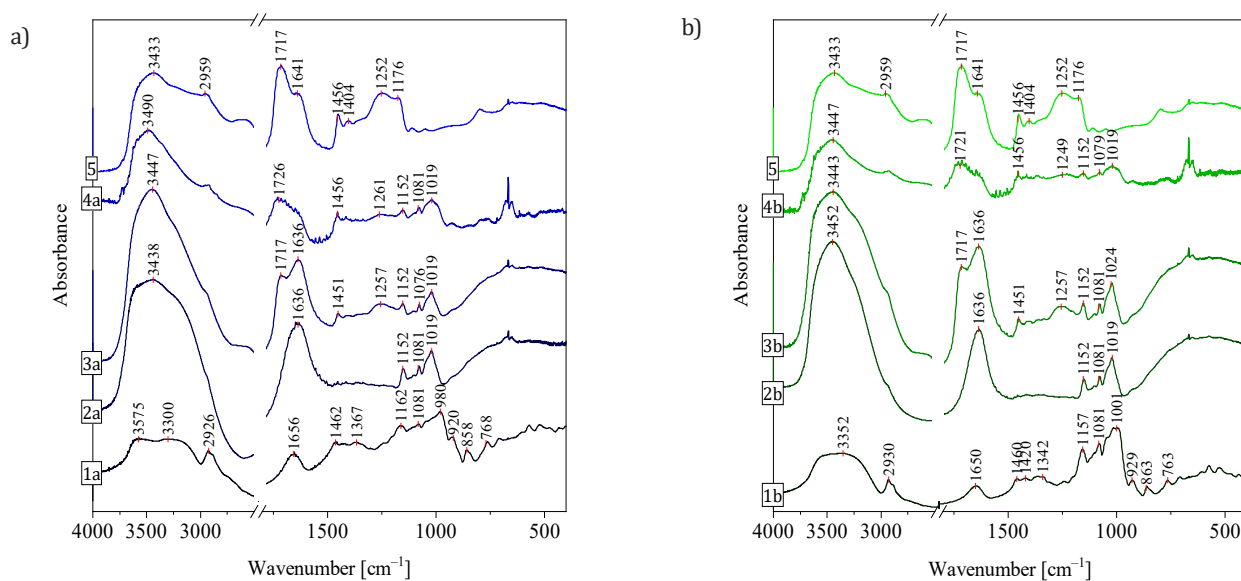


**Fig. 2.** Compilation of IR spectra: $S_P$ (output) (1a), $S_P$ (gelatinised) (2a), H-PA+$S_P$ (3a), H-PA+$S_P$ (dried) (4a), $S_C$ (output) (1b), $S_C$ (gelatinised) (2b), H-PA+$S_C$ (3b), H-PA+$S_C$ (dried) (4b) and PA solution (5)

The band maxima at 760 cm⁻¹, 851 cm⁻¹ and 930 cm⁻¹ confirm the presence of an α-1,4-glycosidic (C–O–C) bond typical for natural starch. Furthermore, on the IR spectra performed for samples 1, 2, 3 and 4, the existence of bands with maxima at wavenumbers 1015 cm⁻¹, 1094 cm⁻¹ and 1163 cm⁻¹ was observed, the formation of which also relates to vibrations characteristic of native starch (vibrations: C–O stretching, C–H bending, C–O and C–C stretching).

In the starch colloidal solutions $S_P$ and $S_C$, the band in the range 3800–3000 cm⁻¹ and the band at ~1636 cm⁻¹ became more intense, which is related to the presence of solvent water (Fig. 2, spectra 2a and 2b). In the wave number range 3600–3000 cm⁻¹, the broad band corresponding to vibrations of the free O-H group (H₂O) and hydrogen bonds does not disappear after drying (spectra 4a and 4b). On the IR spectrum of the starting $S_P$ sample in the region above 3000 cm⁻¹, two maxima related to the presence of intra- and intermolecular bonds were recorded: 3300 cm⁻¹ and 3575 cm⁻¹. After drying, the course of the spectrum changes and shifts of the bands towards the wave number 3490 cm⁻¹ are observed (spectrum 4a). This indicates changes in the hydrogen bonding region, including those occurring in the gelled starch-poly(acrylic acid) – solvent water relationship, and the presence of this band and the shifts in the maxima are probably due to the presence of hydrogen bonds in the hydrogel and the presence of bound water.

The structures of the considered fresh polyacrylate hydrogels H-PA1+$S_P$ and H-PA1+$S_C$ were almost identical (almost without shifts), for example, the bands in the wavenumber range 1250–950 cm⁻¹ and at wavenumber 1636 cm⁻¹ did not change position compared to the $S_P$ and $S_C$ spectra, and these bands on the hydrogel spectra differed only in intensity (Fig. 2, spectra 3a and 3b). The broad band with a maximum at 1637 cm⁻¹ on the colloidal solution spectrum was attributed to water adsorbed in the amorphous regions of the potato starch granule [22].

In dried/conditioned polyacrylate hydrogels involving native starch, no bands, other than those from either the acrylic polymer or the starch, were identified on the spectra, which may indicate that no chemical reaction with the formation of new groups took place between the components under hydrogel preparation conditions. Under conditions of air drying of polyacrylate hydrogels for 24 h, at 25°C and 30–45% humidity – a significant evaporation of solvent took place, as evidenced by changes in the shape and intensity of bands observed on spectra in the wave number range 3800–3000 cm⁻¹. In this range, a decrease in the height of a broad band was observed (Fig. 2, spectra 4a and 4b), but it is still relatively intense and its presence may indicate the existence of hydrogen bonds within the polymer chains – which allows the studied systems to be classified as physical hydrogels.

Table 2 contains data for the detailed identification of the characteristic absorption bands for the obtained IR spectra of the hydrogel H-PA+$S_P$ and H-PA+$S_C$ and their components.

**Table 2**
Characteristic absorption bands in the IR spectra of a sample of H-PA+$S_P$ and H-PA+$S_C$ hydrogel and its components

| Spectrum | | | | | | | | | Vibration | References |
|---|---|---|---|---|---|---|---|---|---|---|
| 1a/$S_P$ | 2a/$S_P$ (colloidal solution) | 3a/ H–PA+$S_P$ (hydrogel) | 4a/ H–PA+SP (dried) | 5/PA | 1b/$S_C$ | 2b/$S_C$ (colloidal solution) | 3b/ H–PA+$S_C$ (hydrogel) | 4b/ H–PA+$S_C$ (dried) | | |
| Wavenumber [cm⁻¹] | | | | | | | | | | |
| 3300 –3575 | 3348 | 3447 | 3490 | 3433 | 3352 | 3452 | 3443 | 3447 | O–H stretching /hydrogen bonding: O–H···O–H; O–H···O=H | [22–24] |
| 2926 | – | – | – | 2959 | 2930 | – | – | – | CH₂ deforming | [25] |
| – | – | 1717 | 1726 | 1717 | – | – | 1717 | 1721 | symmetrical stretching vibrations of the carbonyl group (C=O) | [13] |
| 1656 | 1636 | 1636 | – | 1641 | 1650 | 1636 | 1636 | | deforming H₂O | [23, 24] |
| 1462 | – | 1451 | 1456 | 1456 | 1460 | – | 1451 | 1456 | CH₂ bending symmetric deforming | [26] |
| 1415 | – | – | – | – | 1420 | – | – | – | CH₂ bending symmetric scissoring | [26] |
| 1367 | – | – | – | – | 1342 | – | – | – | C–H bending | [26] |
| – | 1257 | 1261 | 1252 | – | – | 1257 | 1233 | | C–O stretching and | [13] |
| 1162 | 1152 | 1152 | 1152 | 1176 | 1157 | 1152 | 1152 | 1152 | C–O–H deforming | [22–24] |
| 1081 | 1081 | 1076 | 1081 | – | 1081 | 1081 | 1081 | 1078 | C–O, C–C stretching | [23] |
| 980 | 1019 | 1019 | 1019 | – | 1001 | 1019 | 1024 | 1019 | C–H bending | [22, 23] |
| 920 | – | – | – | – | 929 | – | – | – | C–O stretching, CH₂ | [22, 23, 27, 28] |
| 858 | – | – | – | – | 863 | – | – | – | backbone vibration of α-1,4-glycosidic bond (C–O–C) | [23, 24] |
| 768 | – | – | – | – | 763 | – | – | – | C–H, CH₂ deforming | [23] |

### 3.2. Determination of changes occurring in the hydrogel structure under increasing temperature conditions

Structural changes occurring in the obtained polyacrylate hydrogels with gelled native potato and cassava starches, in the presence of increasing temperature in the range of 25–200°C, were recorded online using the reflection technique of attenuated multiple reflectance spectroscopy (ATR-FTIR). The results are summarised as a series of IR spectra in the mid-infrared range 4000–600 cm$^{-1}$ (temperature spectra, Fig. 3). Due to the large number of recorded spectra on the compilation, a discussion of the changes on the individual ATR spectra was omitted. The analysis was carried out by taking into account the disappearance or formation of bands, while isolating the temperature areas of the interpreted changes on the compilation of spectra.

The obtained results of structural studies of H-PA1+S$_P$ and H-PA1+S$_C$ hydrogels carried out under controlled heating conditions allow us to conclude that the prepared hydrogels show similar sensitivity to temperature change in the range 25–200°C.

In the temperature range from 25–200°C, bands presumably corresponding to vibrations of hydroxyl groups are observed on ATR spectra (area A, Figs. 3a and 3b) [29]. At 25°C, in the 3000–3800 cm$^{-1}$ wavenumber range, a single band is present with a maximum at 3296 cm$^{-1}$ for H-PA+S$_P$ and 3350 cm$^{-1}$ for H-PA+S$_C$. As the temperature increases to 125°C on the ATR spectra obtained, the bands in this region do not disappear, but their maxima shift towards lower wavenumbers. This indicates an intensification of the water evaporation process from the hydrogel sample.The process of releasing adsorbed water from the sample in the temperature range 120–150°C is also confirmed by the change in the shape of the band in the region of the wave number 1632 cm$^{-1}$ (area B, Figs. 3a and 3b). At the same time, at temperature 125°C, a band associated with CH$_2$ deforming vibration appears from the slope of the band with a maximum at 2934 cm$^{-1}$ originating from the poly(acrylic acid). In the temperature range up to 200°C, there were structural changes within the hydrogen bonds and evaporation of constitutional water, as evidenced by changes in the intensity and shift of band maxima in the range 3800–3000 cm$^{-1}$, but also by the formation of hydrogen bonding networks in the polymers of the dispersed phase of the hydrogel (poly(acrylic polymer), starch) (Figs. 3a and 3b, area A).

A gradual increase in temperature led to the appearance of bands or an increase in their intensity above 100°C in the wavenumber range 1500–1335 cm$^{-1}$ (Figs. 3a and 3b, area C). At the same time, these are not bands resulting from the formation of new chemical groups, but from the presence of groups characteristic of the poly(acrylic acid) from the polymeric system due to evaporation of the dispersion phase.

Changes in the 800–750 cm$^{-1}$ range above 100°C indicate of structural changes within the starch monomers, and a shift in the maximum may indicate the onset of thermal degradation of the hydrogel (Figs. 3a and 3b, area D).

Table 3 presents an analysis of the characteristic absorption bands occurring in the areas highlighted in Figure 3 on the ATR-FTIR spectra of H-PA+S$_P$ and H-PA+S$_C$ hydrogels.
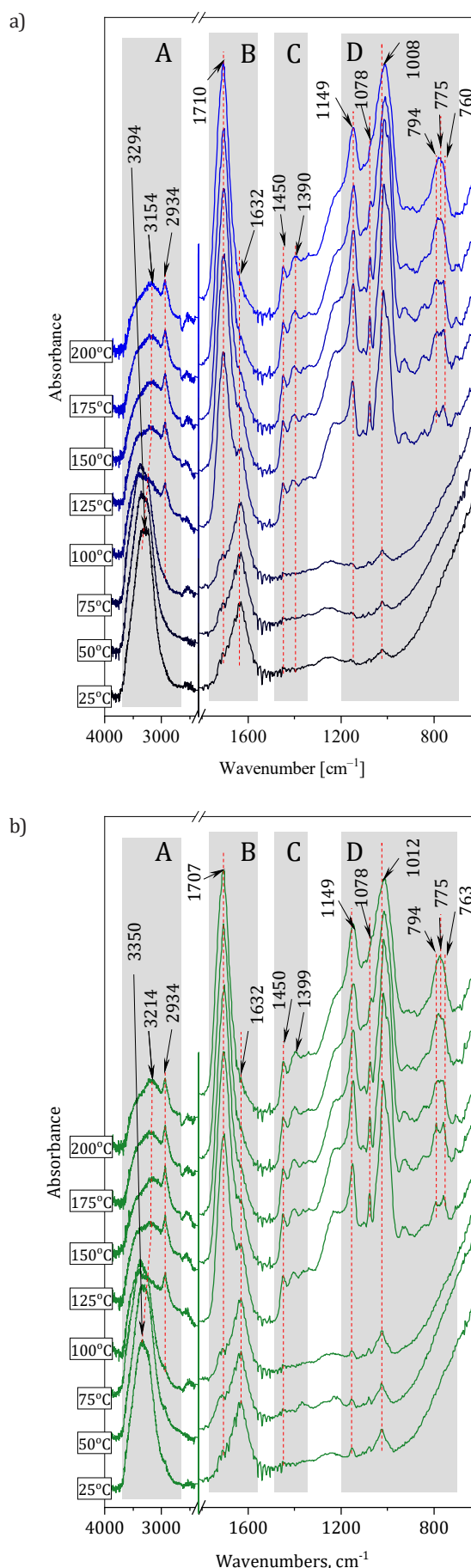


**Fig. 3.** A compilation of infrared spectra (ATR-FTIR) in the temperature range from 25–200°C: a) H-PA+S$_P$, b) H-PA+S$_C$

**Table 3**
Characteristic absorption bands in the IR spectra of polymeric hydrogel samples H-PA+S$_P$ and H-PA+S$_C$ and their assignment to the respective structure elements

| Area | Wavenumber range [cm$^{-1}$] | Temperature range [°C] | Vibration | Observed changes |
|------|------------------------------|------------------------|-----------|------------------|
| A | 3800–3000 | 25–200 | hydrogen bonds: OH | decrease in intensity of the band with a maximum of 3294 cm$^{-1}$; above 100°C shift of the maximum to 3154 cm$^{-1}$ of the band |
|  |  | 100–200 | C–H stretching | appearance of a band with a maximum at 2934 cm$^{-1}$ |
| B | 1800–1545 | 25–200 | deforming H$_2$O | fading of the band at 1632 cm$^{-1}$ |
|  |  | 100–200 | C=O stretching | increase in intensity of the band with a maximum at 1710 cm$^{-1}$ |
| C | 1500–1335 | 100–200 | C–H symmetric bending | shift of the band maximum ~1390 cm$^{-1}$ |
|  |  |  | CH$_2$ symmetric bending deforming | band intensity change of 1450 cm$^{-1}$ |
| D | 1200–600 | 25–200 | (C–O)H | appearance of the band at 1149 cm$^{-1}$ |
|  |  | 100–200 | C–H bending | disappearance of the band at 1078 cm$^{-1}$ |
|  |  |  | C–O stretching, CH$_2$ | change in intensity and shape of the band at ~1010 cm$^{-1}$ |
|  |  |  | C–O–C vibrations in the starch monomer ring | change in intensity and shape of the band with maxima at 794 cm$^{-1}$ and ~760 cm$^{-1}$ (disappearance of two maxima with formation of one at 775 cm$^{-1}$) |

## 4. CONCLUSIONS

On the basis of the research carried out and the analysis of the results obtained, the following conclusions can be drawn:

- the obtained results of structural studies conducted with the transmission technique (FTIR) confirm that, despite the different biological origin of natural potato and cassava starches, their chemical structure is very similar. The differences are manifested in the intensity of characteristic bands, e.g. those attributed to O–H vibrations (the presence of both intra- and intermolecular hydrogen bonds);

- the chemical structure of prepared polyacrylate hydrogels, irrespective of the biological source of the natural starch used, is almost identical; slight differences in the structure are manifested by the presence and intensity of characteristic bands, however, their location is the same in each case (within the measurement error limit);

- by comparing the IR spectra of fresh and dried hydrogel, a change in intensity and a shift in band maxima in the range of wavenumbers 3800–3000 cm$^{-1}$ was found, which testifies to the physical nature of the process of the transformation of liquid hydrogel to a solid form;

- thanks to the application of the ATR-FTIR technique, it was possible to assess differences in the sensitivity of hydrogels with both potato and cassava starch to an increase in temperature up to 200°C; in both cases, structural changes occurring under increasing temperature conditions followed a similar pattern, irrespective of the type of natural starch used; at a temperature of approximately 200°C, changes were noted that could be linked to thermal degradation of the bonds in the hydrogel.

## REFERENCES

[1] Tyliszczak B. & Pielichowski K. (2007). Charakterystyka matryc hydrożelowych – zastosowania biomedyczne superabsorbentów polimerowych. *Czasopismo Techniczne. Chemia*, R. 104, 159–167.

[2] Bogunia A. & Król J. (2018). *Materiał hydrożelowy – nowa podstawa dla tkanek organizmu*. https://www.innowacyjnystart.pl/ludzie/195-material-hydrozelowy-nowa-podstawa-dla-tkanek-organizmu [accessed: 12.08.2023].

[3] Kazimierska-Drobny K. (2011). *Symulacja procesów chemo-mechanicznych w porowatych żelach i identyfikacja parametrów modelu*. Uniwersytet Kazimierza Wielkiego w Bydgoszczy [PhD thesis]. https://www.ippt.pan.pl/repository/doktoraty/open/2012kazimierska_doktorat.pdf [accessed: 12.08.2023].

[4] Pluta J. & Karolewicz B. (2004). Hydrogels: Properties and application in the technology of drug form. I: The characteristic hydrogels. *Polimery w Medycynie*, 34(2), 3–19.

[5] Qamruzzaman M., Ahmed F. & Mondal M.I.H. (2022). An overview on starch-based sustainable hydrogels: Potential applications and aspects. *Journal of Polymers and the Environment*, 30, 19–50. Doi: https://doi.org/10.1007/s10924-021-02180-9.

[6] *Material extrusion – FDM* (n.d.). Retrieved from: https://make.3dexperience.3ds.com/processes/material-extrusion [accessed: 22.06.2022].

[7] Li J., Wu C., Chu P.K. & Gelinsky M. (2020). 3D printing of hydrogels: Rational design strategies and emerging biomedical applications. *Materials Science and Engineering R: Reports*, 140, 100543. Doi: https://doi.org/10.1016/j.mser.2020.100543.

[8] Li L., Zhang P., Zhang Z., Lin Q., Wu Y., Cheng A., Lin Y., Thompson C.M., Smaldone R.A. & Ke C. (2018). Hierarchical co-assembly enhanced direct ink Writing. *Angewandte Chemie International Edition*, 57(18), 5105–5109. Doi: https://doi.org/10.1002/anie.201800593.

[9] Kijeński J., Migdał A., Rejewski P. & Kędziora A. (2016). Przemysłowa synteza kwasu akrylowego i akrylanów – droga do eliminacji białych plam w obszarze wytwórczym polskiego przemysłu chemicznego. *Polimery*, 61(10), 702–709. Doi: https://doi.org/10.14314/polimery.2016.702.

[10] Szymańska J. & Bruchajzer E. (2012). Kwas akrylowy. Dokumentacja dopuszczalnych wielkości narażenia zawodowego. *Podstawy i Metody Oceny Środowiska Pracy*, 4(74), 69–97. https://yadda.icm.edu.pl/baztech/element/bwmeta1.element.baztech-a6f80ccf-5a8b-4711-b3f9-ae86f718d27d/c/Szymanska_kwas.pdf [accessed: 12.08.2023].

[11] Grabowska B., Pilch-Pitera B., Kaczmarska K., Trzebicka B., Mendrek B., Drożyński D. & Łątka P. (2015). Właściwości kompozycji poli(kwas akrylowy)/modyfikowana skrobia stosowanej jako nowe spoiwo polimerowe. *Polimery*, 60(3), 179–185. Doi: https://doi.org/10.14314/polimery.2015.179.

[12] Grabowska B., Holtzer M., Dańko R. Górny M., Bobrowski A. & Olejnik E. (2013). New BioCo binders containing biopolymers for foundry industry. *Metalurgija*, 52(1), 47–50. https://www.researchgate.net/publication/259558063.

[13] Grabowska B. (2013). *Nowe spoiwa polimerowe w postaci wodnych kompozycji z udziałem poli(kwasu akrylowego) lub jego soli i modyfikowanego biopolimeru*. Kraków: Wydawnictwo Naukowe AKAPIT.

[14] Dąbrowska A. & Jagiello B.U. (2009). Drogi rozkładu skrobi w roślinach. *Kosmos. Problemy Nauk Biologicznych*, 58(282–283), 211–220. http://kosmos.icm.edu.pl/PDF/2009/211.pdf.

[15] Tomasik P. (2004). *Chemical and Functional Properties of Food Saccharides*. London: CRC Press LLC.

[16] Wang S. & Copeland L. (2013). Molecular disassembly of starch granules during gelatinization and its effect on starch digestibility: a review. *Food & Function*, 4(11), 1564–1580. Doi: https://doi.org/10.1039/c3fo60258c.

[17] Kaczmarska K. (2017). *Sól sodowa karboksymetyloskrobi (CMS-Na) jako materiał do zastosowania w technologii mas formierskich*. Kraków: Akademia Gorniczo-Hutnicza [PhD thesis].

[18] Lewandowicz G. & Mączyński M. (1990). Chemiczna modyfikacja skrobi. Cz. I. Modyfikacja skrobi ziemniaczanej. *Chemik*, 1, 9–13.

[19] Ma X., Wei R., Cheng J., Cai J. & Zhou J. (2011). Synthesis and characterization of pectin/poly (sodium acrylate) hydrogels. *Carbohydrate Polymers*, 86(1), 313–319. Doi: https://doi.org/10.1016/J.CARBPOL.2011.04.089.

[20] Souda P. & Sreejith L. (2013). Poly (acrylate -acrylic acid-co-Maleic acid) hydrogel: A cost effective and efficient method for removal of metal ions from water. *Separation Science and Technology*, 48(18), 2795–2803. Doi: https://doi.org/10.1080/01496395.2013.809106.

[21] Sadeghi M. & Soleimani F. (2012). Synthesis of pH-sensitive hydrogel based on starch-polyacrylate superabsorbent. *Journal of Biomaterials and Nanobiotechnology*, 3(2A), 310–314. Doi: https://doi.org/10.4236/jbnb.2012.322038.

[22] Kizil R., Irudayaraj J. & Seetharaman K. (2002). Characterization of irradiated starches by using FT-Raman and FTIR spectroscopy. *Journal of Agricultural and Food Chemistry*, 50(14), 3912–3918. Doi: https://doi.org/10.1021/jf011652p.

[23] Schuster K.C., Ehmoser H., Gapes J.R. & Lendl B. (2000). On-line FT-Raman spectroscopic monitoring of starch gelatinisation and enzyme catalysed starch hydrolysis. *Vibrational Spectroscopy*, 22(1–2), 181–190. Doi: https://doi.org/10.1016/S0924-2031(99)00080-6.

[24] Sekkal M., Dincq V., Legrand P. & Huvenne J.P. (1995). Investigation of the glycosidic linkages in several oligosaccharides using FT-IR and FT Raman spectroscopies. *Journal of Molecular Structure*, 349, 349–352. Doi: https://doi.org/10.1016/0022-2860(95)08781-P.

[25] Budarin V., Clark J.H., Hardy J.J.E., Luque R., Milkowski K., Tavener S.J. & Wilson A.J. (2006). Starbons: New starch-derived mesoporous carbonaceous materials with tunable properties. *Angewandte Chemie – International Edition*, 45(23), 3782–3786. Doi: https://doi.org/10.1002/anie.200600460.

[26] Abdullah A.H.D., Chalimah S., Primadona I. & Hanantyo M.H.G. (2018). Physical and chemical properties of corn, cassava, and potato starchs. *IOP Conference Series: Earth and Environmental Science*, 160, 012003. Doi: https://doi.org/10.1088/1755-1315/160/1/012003.

[27] Vasko P.D., Blackwell J. & Koenig J.L. (1971). Infrared and Raman spectroscopy of carbohydrates. Part I: Identification of O-H and C-H related vibrational modes for D-glucose, maltose, cellobiose, and dextran by deuterium-substitution methods. *Carbohydrate Research*, 19, 297–310.

[28] Vasko P.D., Blackwell J. & Koenig J.L. (1972). Infrared and Raman spectroscopy of carbohydrates. Part II: Normal and coordinate analysis of α-D-glucose. *Carbohydrate Polymers*, 23, 407–416. Doi: https://doi.org/10.1016/S0008-6215(00)82690-7.

[29] Zaltariov M.F., Filip D., Varganici C.D. & Macocinschi D. (2018). ATR-FTIR and thermal behavior studies of new hydrogel formulations based on hydroxypropyl methylcellulose/poly(acrilic acid) polymeric blends. *Cellulose Chemistry and Technology*, 52(7–8), 619–631. https://www.cellulosechemtechnol.ro/pdf/CCT7-8(2018)/p.619-631.pdf [accessed: 12.08.2023].